Role of Gd^{3+} and Ho^{3+} doping on the structure, physical properties and applications of ZnO

M. M. Arman[1] · Alaa AL-Rahman Gamal[2]

Abstract

ZnO, $Zn_{0.97}Gd_{0.03}O$ and $Zn_{0.97}Ho_{0.03}O$ were prepared via a citrate auto-combustion method. X-ray diffraction (XRD) demonstrated that the investigated nanoparticles were prepared in a hexagonal structure, with crystallite sizes averaging between 12 and 60 nm. The morphology of the samples is illustrated by the field emission scanning electron microscope (FESEM) images. The paramagnetic behavior of the investigated nanoparticles is demonstrated by VSM. The value of the optical band gap (E_g) of $Zn_{0.97}Gd_{0.03}O$ was higher than the E_g of ZnO due to the Moss–Burstein effect. Heavy metal Cd^{2+} ions from water are effectively adsorbed by rare earth-doped ZnO. At pH $= 8$, $Zn_{0.97}Ho_{0.03}O$ exhibits a maximum removal efficiency of 91%. The Freundlich isotherm model fits the experimental results well.

Keywords ZnO · $Zn_{0.97}Gd_{0.03}O$ · $Zn_{0.97}Ho_{0.03}O$ · The removal efficiency · Nanoparticles

1 Introduction

Transition metal oxides, such as ZnO nanoparticles, have numerous properties, including high stability, non-toxicity, safety, ease of preparation, n-type semiconductor, and low cost [1]. ZnO nanoparticles have various applications, such as piezoelectric devices, gas sensors, photocatalysts, biosensors, anti-UV additives, electrodes, and heavy metal removal [2–5]. Due to its high surface area, which can efficiently adsorb HM, ZnO exhibits a significant capability to remove heavy metals from water [6].

Doping ZnO changes its properties, including its electronic, optical, magnetic, and morphology properties, as well as its applications [3, 7]. Doping ZnO with rare earth elements enhances its characteristics due to the tiny crystal field splitting, electronic structure, and partially filled 4f orbitals of rare earth metals [8].

Heavy metals (HM) are elements that are characterized by a large density greater than 6 g/cm^3 and have a high toxic effect even in a small amount [9]. Due to their toxicity, lack of biodegradability, and detrimental effects on both people and plants. HM such as Cr^{6+}, Ni^{2+}, and Pb^{2+} in water constitute a significant environmental threat [10, 11]. There are many sources of Cd^{2+}, such as paints, alloying, batteries, electroplating, fertilizers, and metal smelting [12]. The harmful effects of Cd^{2+} are bone tumors, renal dysfunction, high blood pressure, and pulmonary problems [13].

The water treatment can be performed by different techniques, such as membrane technologies [14], photocatalytic degradation [15], the precipitation method [16], oxidation–reduction [17], and flotation [18]. The adsorption process is the transition of the heavy metals (adsorbate) from the aqueous phase to nanoparticles (adsorbent), which form an atomic or molecular layer on the adsorbent [19, 20]. The purification of water using the adsorption method is more effective due to its simplicity, cost-effectiveness, and no sludge. There are various factors that affect the adsorption process, such as the pH value of the solution, contact time, concentration of HM, and magnetic behavior of the adsorbent. The magnetic nanoparticles can be easily separated from the solution after adsorption using an external magnet.

Many studies have shown that the presence of Ho^{3+} and Gd^{3+} ions in nanoparticles increases the efficiency of HM removal from water [21, 22]. These are due to the increased surface area to volume ratio and the increased number of active sites on the surface of the adsorbent. M.M. Arman

✉ M. M. Arman
    mmarmsci@cu.edu.eg; mmarmsci@gmail.com

1   Materials Science Lab (1), Physics Department, Faculty of Science, Cairo University, Giza, Egypt

2   Biophysics Group, Physics Department, Faculty of Science, Ain Shams University, Cairo, Egypt

[21] reported that the $Sm_{0.95}Ho_{0.05}FeO_3$ has a good removal efficiency of lead ions from water, with the removal capacity reaching 99% at pH = 8. E.E. Ateia et al. [22] prepared $GdFe_{0.8}Co_{0.2}O_3$, which had a 98% adsorption efficiency of lead from water at pH 5. In order to increase the removal efficiency of the ZnO, both Ho^{3+} and Gd^{3+} ions were chosen as dopants in ZnO nanoparticles.

The current study shows the influence of doping ZnO with RE. Using the citrate auto-combustion technique, the samples ZnO, $Zn_{0.97}Gd_{0.03}O$, and $Zn_{0.97}Ho_{0.03}O$ were synthesized in a single-phase hexagonal structure. This study aimed to determine how the doping of Gd^{3+} and Ho^{3+} ions affected the structure, morphology, and physical properties of ZnO, in addition to evaluating the effects of Gd^{3+} and Ho^{3+}-doping ZnO on the adsorption of Cd^{2+} from water.

2 Experimental techniques

2.1 Materials used

All of the chemicals used to create ZnO, $Zn_{0.97}Gd_{0.03}O$, and $Zn_{0.97}Ho_{0.03}O$ are of annular purity (purity 99.9%). The zinc nitrate, Ho nitrate, Gd nitrate, and citric acid are purchased from Sigma Aldrich Company.

2.2 The preparation of nanosamples

ZnO, $Zn_{0.97}Gd_{0.03}O$, and $Zn_{0.97}Ho_{0.03}O$ were synthesized using the citrate combustion technique [23]. The stoichiometric ratios of Zn nitrate, Ho nitrate, Gd nitrate, and citric acid were dissolved in distilled water. The nitrate to citrate ratio is 1:1. Using the ammonia solution, the pH of the solution was adjusted to 7. The samples were stirred and heated at 80 °C for 1 h, then heated at 200 °C till the liquid phase evaporated and the ash was produced. The ash was ground for an hour using an agate mortar, and the resulting powder was calcined for three hours at 550 °C using a rate of heating and cooling of 5 °C/min.

2.3 Characterization and measurement of samples

Phase identification was investigated, and the lattice size and lattice parameters were determined using XRD (a Bruker Advance D8 diffractometer). The morphology of the materials was demonstrated using FESEM (model Quanta 250). The magnetization of the synthesized nanoparticles was investigated via VSM (9600-1 LDJ, USA). Using a UV/visible/NIR spectrophotometer (JASCO Corp., V-570), the
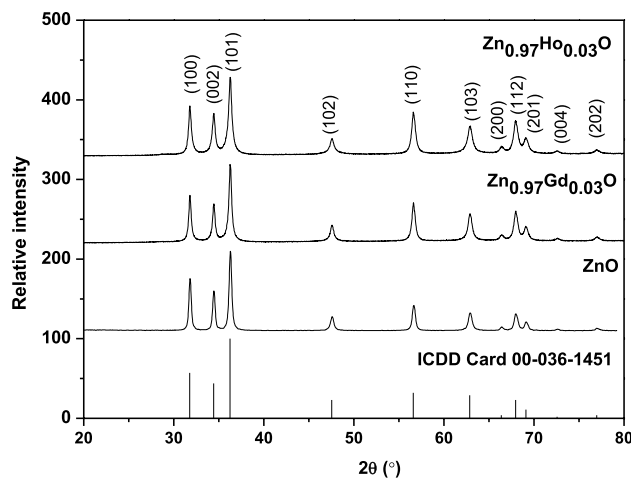

Fig. 1 XRD of the prepared nanoparticles

optical transition type and optical band gap values for the materials were determined.

2.4 The removal of Cd^{2+} ions

A standard solution of Cd^{2+} (50 ppm) was prepared to study the removal of these ions from water. In a beaker with 10 mL of the standard solution, 0.02 g of the sample was added. Ammonia or nitric acid solutions are used to adjust the solution's pH. The solution was placed on an electric shaker (Orbital Shaker SO1) at room temperature and stirred at 180 rpm for one hour. 10 mL of the solution was filtered via a syringe filter. Inductively coupled plasma (ICP, spectrometry, Prodigy7) was used to calculate the number of Cd^{2+} ions in the aqueous medium.

Equations (1) and (2) were used to compute the Cd^{2+} efficiency (η) and the adsorption capacity (q) [21].

$$\eta = \frac{C_i - C_e}{C_i} \times 100 \tag{1}$$

$$q = \frac{(C_i - C_e)V}{m}, \tag{2}$$

where V is the volume of the Cd^{2+} solution, m is the mass of ZnO, and C_e and C_i are the final and initial concentrations of the Cd^{2+} solution, respectively.

3 Results and discussion

XRD results proved that the synthesized samples have a one-phase hexagonal structure and were indexed with ICDD card 00-036-1451 as shown in Fig. 1. The main peak was indexed

at $2\theta = 36.3°$ for the lattice peak 101. According to the following equation, the lattice parameters of the investigated nanoparticles were calculated:

$$\frac{1}{d^2} = \left[\frac{4}{3}(h^2 + k^2 + hk) + l^2\left(\frac{a}{c}\right)^2\right]\frac{1}{a^2}, \qquad (3)$$

where h, k, and l are the Miller indices, while d is the distance between the planes. Table 1 contains the lattice constants a, b, and c. The unit cell volume (V), and the theoretical density (D_x) were calculated according to the following equations:

$$V = a^2 c \qquad (4)$$

$$Dx = \frac{ZM}{N_A V}, \qquad (5)$$

where M refers to the molecular weight, Z (Z = 2) denotes the molecule's number in a unit cell and N_A is Avogadro's number. The crystallite size (D) of rare earth-doped ZnO was calculated using the well-known Scherer's equation [24].

$$D = \frac{0.94\lambda}{\beta \cos\theta}, \qquad (6)$$

where λ denotes the X-ray wavelength and β refers to the full width at half the maximum intensity. The crystallite size (D) values for the samples ZnO, $Zn_{0.97}Ho_{0.03}O$, and $Zn_{0.97}Gd_{0.03}O$ are 12.48 nm, 51.18 nm, and 60.20 nm, respectively. The replacement of Zn ions with small ionic radii ($r_{Zn} \sim 0.74$ Å) by Gd³⁺ and Ho³⁺ with high ionic radii ($r_{Gd} \sim 0.938$ Å and $r_{Ho} \sim 0.995$ Å) resulted in an increase in the D due to rare earth doping [25]. The samples defects are indicated by dislocated density (δ) which was estimated via the following equation and listed in Table 1 [26, 27].

$$\delta = \frac{1}{D^2} \qquad (7)$$

The Zn–O bond length (L) of samples was altered with the RE doping due to changes in the lattice parameters. The dependence of L on the RE elements can be determined using Eq. (8) [28].

$$L = \sqrt{\left[\frac{a^3}{3} + \left(\frac{1}{2} - u\right)^2 c^2\right]}, \qquad (8)$$

where u is the potential parameter related to the hexagonal structure, which can be calculated from Eq. (9) [28].

$$u = \frac{a^2}{3c^2} + 0.25 \qquad (9)$$

Table 1 contains values of L for the synthesized nanoparticles, which decreased for the $Zn_{0.97}Gd_{0.03}O$ and $Zn_{0.97}Ho_{0.03}O$ owing to the incorporation of Gd and Ho in the zinc oxide lattice, where the ionic radii of RE are greater than those of ZnO, resulting in a reduction in the bond length of Zn–O [29].

The samples morphology was investigated using FESEM images. Figure 2 shows that the ZnO, $Zn_{0.97}Gd_{0.03}O$, and $Zn_{0.97}Ho_{0.03}O$ samples have irregular morphological structures. The small particles were agglomerated, forming large clusters. There is a slight variation in the agglomeration degree between the samples. The agglomeration occurs as a result of the absence of a surfactant agent during the preparation [30].

The hysteresis loops of the ZnO, $Zn_{0.97}Gd_{0.03}O$, and $Zn_{0.97}Ho_{0.03}O$ samples are illustrated in Fig. 3. The hysteresis loops demonstrate the paramagnetic properties of the prepared nanoparticles. In the inset of Fig. 3, H_c and M_r for ZnO, $Zn_{0.97}Gd_{0.03}O$, and $Zn_{0.97}Ho_{0.03}O$ are shown. The values of M_m, M_r, H_c, and the squareness ratio are reported in Table 2. The anisotropy constant (K) of the investigated samples was calculated using Eq. (10).

$$K = \frac{H_C \times M_S}{0.96} \qquad (10)$$

The bulk of ZnO is characterized by diamagnetic properties [31, 32]. Many researchers claim that ZnO has paramagnetic [33] or weak ferromagnetic properties at the nanoscale [34]. In a very small dimension of ZnO, the magnetic properties originated for many reasons, such as:
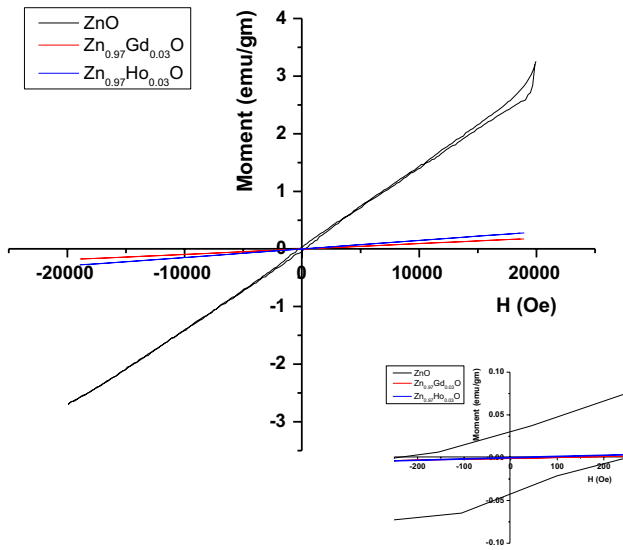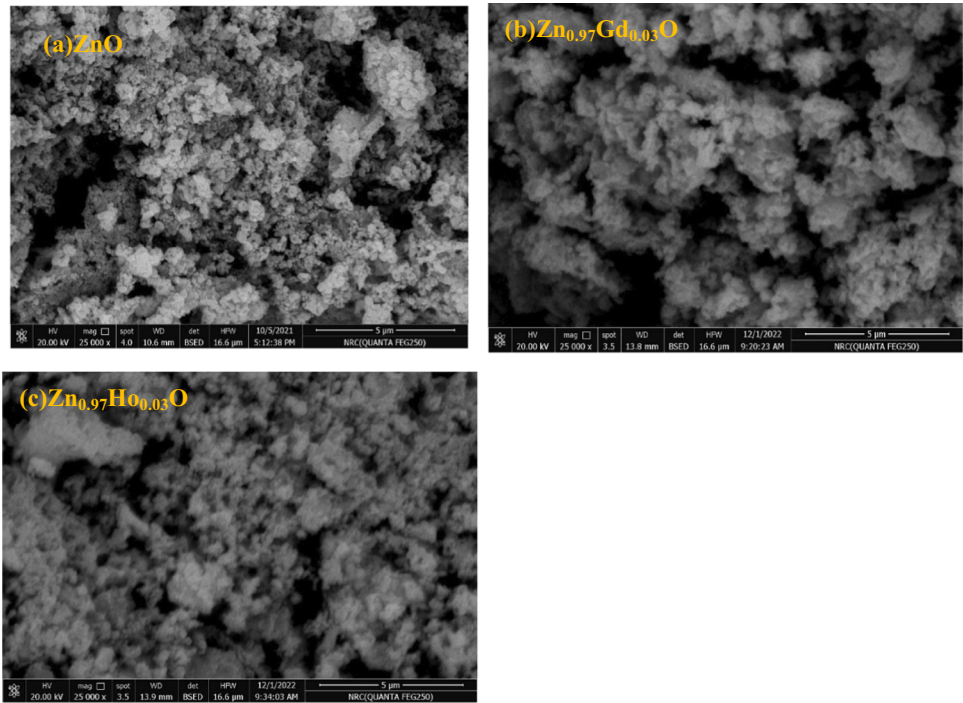
1. the point defects in zinc oxide, like the Zn interstitials and vacancies of oxygen ions [34–36].
2. the presence of more than one phase in the ZnO matrix.

The investigated samples were prepared in a single phase, according to the XRD data, so the last reason does not apply to the investigated samples. Because of the increased particle size, the magnetization of RE-doped samples is small, resulting in a decrease in magnetic behavior.

Table 1 The lattice parameters, theoretical density (D_x), crystallite size (D), dislocated density (δ) and bond length (L) for the samples

Samples	a(Å)	b(Å)	c(Å)	V(Å³)	D_x (g/cm³)	D (nm) (XRD)	$\delta \times 10^{-3}$ (nm)$^{-2}$	L (Å)
ZnO	3.253	3.253	5.207	55.085	4.906	12.48	6.421	1.9793
$Zn_{0.97}Gd_{0.03}O$	3.249	3.249	5.206	54.955	5.084	60.20	0.276	1.9774
$Zn_{0.97}Ho_{0.03}O$	3.251	3.251	5.207	55.032	5.091	51.18	0.382	1.9784

Fig. 2 FESEM images for ZnO, $Zn_{0.97}Gd_{0.03}O$, and $Zn_{0.97}Ho_{0.03}O$

Fig. 3 The magnetic hysteresis loops of the samples

The band gap (E_g) can be determined using the Kubelka–Munk (K–M) equation: [37]
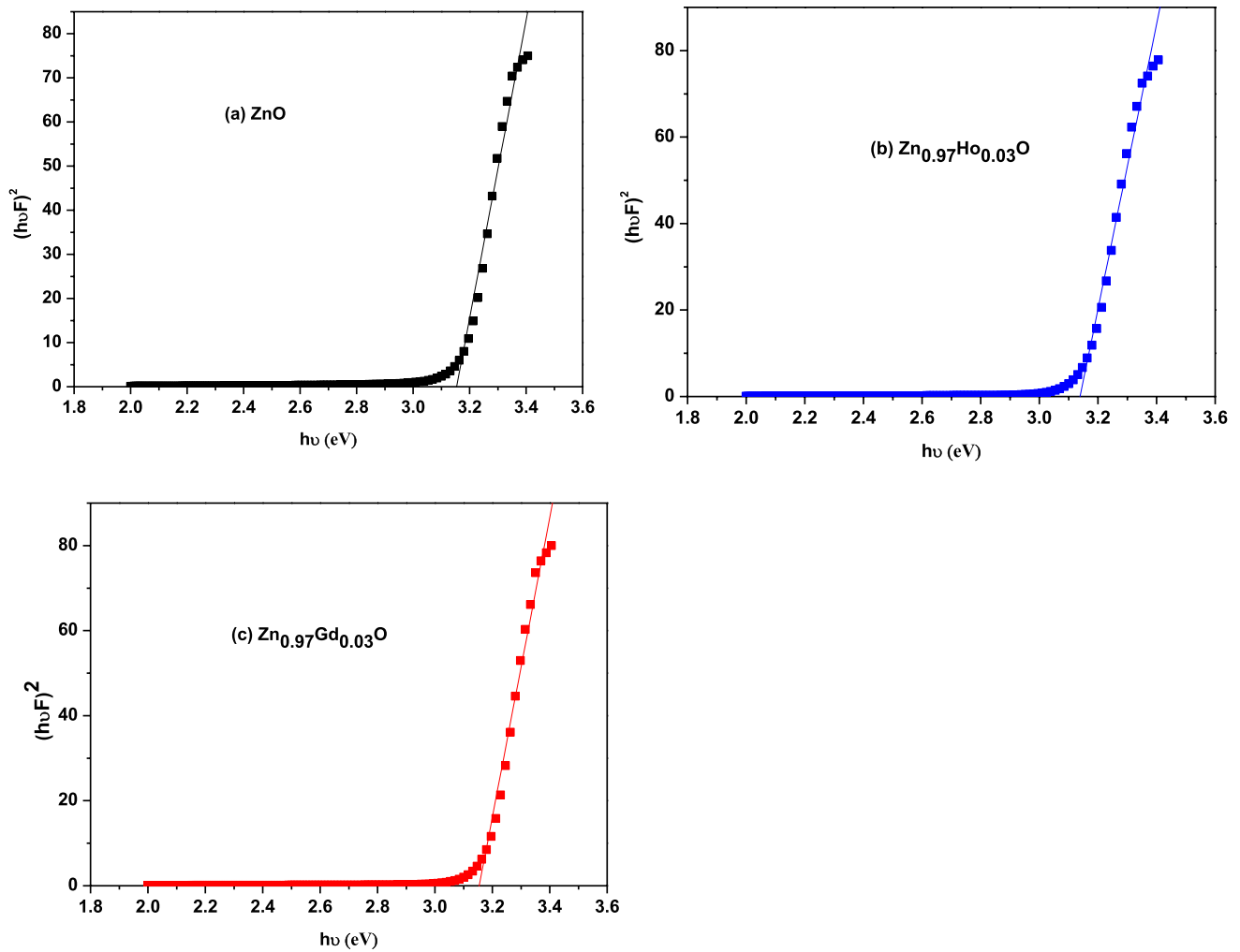
$$F(R) = \frac{(1-R)^2}{2R}, \tag{11}$$

where F (R) is the K–M function related to the extinction coefficient (α) and R refers to the reflectance.

Tauc's equation [38, 39] can be used to calculate the type of optical transition and the E_g values.

$$(F(R)\,h\upsilon)^2 \approx A\left(h\upsilon - E_g\right)^n, \tag{12}$$

where A denotes a constant and $h\upsilon$ refers to the energy of the photon. The type of transition depends on the value of the exponent, which can be either indirect allowed (n = 2) and direct allowed (n = 1/2).

Figure 4 depicts the relationship between $(F(R)\,h\upsilon)^2$ and $h\upsilon$. The E_g values can be calculated from the intercept with the x-axis and are reported in Table 3. E_g for the samples are strongly influenced by shifting the conduction band (CB) rather than the valence band (VB) due to the hole's effective mass in VB being larger than that of the electrons in CB

Table 2 The remanence magnetization (M_r), the maximum magnetization (M_m), the coercivity (H_c), the squareness ratio, and the anisotropy constant (K) for ZnO and RE-doped samples

Samples	M_m (emu g^{-1})	M_r (emu g^{-1})	H_c Oe	K (emu Oe g^{-1})	Squareness
ZnO	3.257	36.4×10^{-3}	248.02	841.46	11.18×10^{-3}
$Zn_{0.97}Ho_{0.03}O$	0.277	0.446×10^{-3}	30.28	8.74	1.61×10^{-3}
$Zn_{0.97}Gd_{0.03}O$	0.175	0.025×10^{-3}	4.78	0.87	0.14×10^{-3}

Fig. 4 Tauc plots for **a** ZnO, **b** Zn$_{0.97}$Ho$_{0.03}$O, and **c** Zn$_{0.97}$Gd$_{0.03}$O nanoparticles

Table 3 The energy gap for the investigated samples

Samples	E$_g$ (eV)
ZnO	3.154
Zn$_{0.97}$Ho$_{0.03}$O	3.138
Zn$_{0.97}$Gd$_{0.03}$O	3.157

[40]. Many researchers, including Kasirajan [27] and Wang [41], agree that the value of E$_g$ for ZnO is 3.154 eV. The small addition of Gd at the expense of Zn in ZnO leads to a very small increase in E$_g$. Kasirajan [27] concluded that the elevation in E$_g$ of Gd-doped zinc oxide thin film was due to the elevation in the density and grain size of ZnO. Another reason for increasing the Eg of Zn$_{0.97}$Gd$_{0.03}$O rather than the value of ZnO is the Moss–Burstein effect [40]. Because the Gd atoms are donors, Zn$_{0.97}$Gd$_{0.03}$O can be represented as an n-type semiconductor. According to many researchers, including Kabongo, the energy gap of Zn$_{0.97}$Ho$_{0.03}$O was greater than that of ZnO [42].
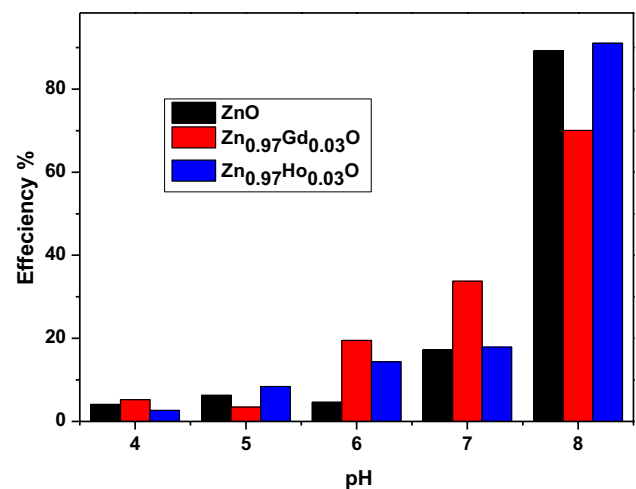
Fig. 5 The relation between the removal efficiency of Cd^{2+} ions and the pH values for the ZnO, Zn$_{0.97}$Gd$_{0.03}$O and Zn$_{0.97}$Ho$_{0.03}$O

The absorption of heavy metals is strongly influenced by the pH of the solution, and the surface charge of nanoparticles varies with pH [43]. Figure 5 depicts the relationship between the efficiency of cadmium ion removal and the pH of the solution. According to Fig. 5, the overall trend is that the removal efficiency rises with increasing pH. At low pH, more H^+ ions compete with Cd^{2+} ions on the NPs surfaces, so Cd^{2+} ion adsorption is low. Because more OH^- ions are present in the solution in the alkaline medium at pH = 8, more Cd^{2+} ions precipitate in the hydroxide form. Doping ZnO with rare earth elements (Gd and Ho) improves water purification from Cd^{2+} ions. While at pH = 7, the removal efficiency (η) of ZnO nanoparticles is 17%, and η increases to 34% for $Zn_{0.97}Gd_{0.03}O$. While the maximum removal efficiency is 91% for the $Zn_{0.97}Ho_{0.03}O$ nanoparticles at pH = 8. The XRD of the samples assured that the samples were prepared in nanoscale, which is characterized by a large surface area to volume ratio. As the surface area of the adsorbent increases, the adsorption active sites will increase, as will the removal efficiency. The substitution of Gd^{3+} or Ho^{3+} for Zn^{2+} results in the formation of active adsorption sites and an increase in HM removal efficiency [44].

The isotherm models were used to study the data on the removal of Cd^{2+} ions from water. The Freundlich and Langmuir models were described using Eqs. (13) and (14), respectively.

$$\frac{C_e}{q_e} = \frac{1}{q_m K_L} + \frac{C_e}{q_m} \tag{13}$$

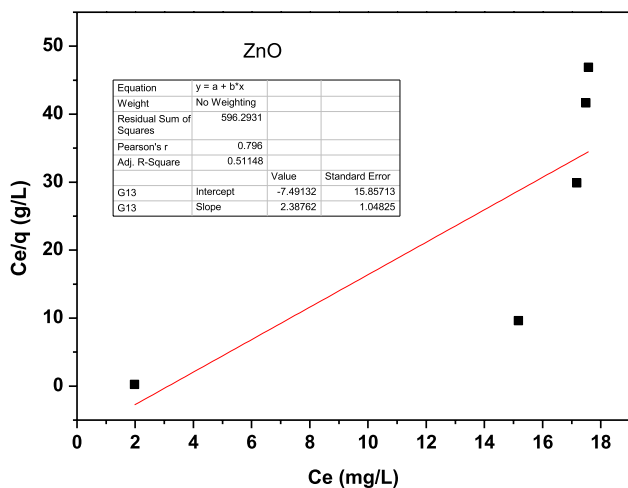$$q_e = K_f C_e^{\frac{1}{n}}, \tag{14}$$

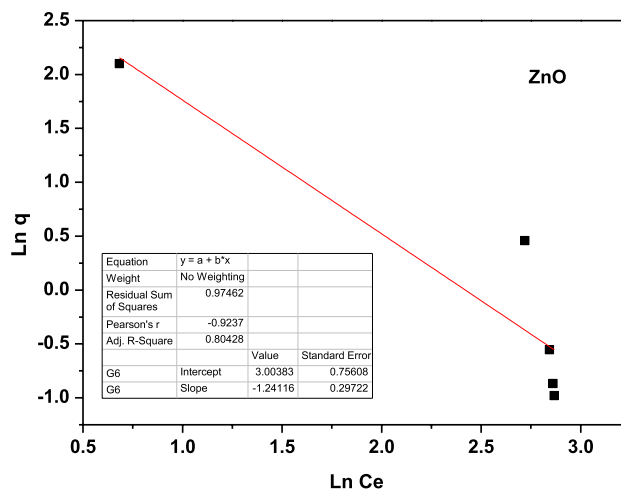**Fig. 6** The Langmuir isotherm model fitting for ZnO

Fig. 7 The Freundlich isotherm model fitting for ZnO

where $\frac{1}{n}$ is the adsorption intensity, K_f denotes the Freundlich constant, while q_m and K_L are the Langmuir constants.

Figure 6 illustrates the relationship between Ce/q and Ce, which represents the Langmuir isotherm model. Figure 7 shows how Lnq is dependent on Ln Ce, which represents the Freundlich model. The Freundlich constant is listed in Table 4.

Table 4 lists the Langmuir constant, the adsorption intensity, and the correlation coefficient (R^2) values for the two isotherm models. The Freundlich model has a higher value of R^2 for all samples. Thus, the Freundlich model can most accurately predict the experimental data.

4 Conclusion

The rare earth-doped ZnO was synthesized using the citrate auto-combustion technique. XRD confirmed that the crystallite size increased with rare earth doping. FESEM revealed irregular morphological structures of the prepared nanoparticles. The paramagnetic characteristics of ZnO, $Zn_{0.97}Ho_{0.03}O$, and $Zn_{0.97}Gd_{0.03}O$ were confirmed by VSM. By doping ZnO with RE, the optical band gap (E_g) can be altered. E_g increased by Gd doping from 3.154 eV for ZnO to 3.157 eV for $Zn_{0.97}Gd_{0.03}O$, while E_g decreased by

Table 4 The Langmuir constant, the adsorption intensity, and the correlation coefficient (R^2) for the Langmuir and Freundlich models

Samples	Freundlich model		Langmuir model	
	R^2	$\frac{1}{q_m}(mg/g)^{-1}$	R^2	$\frac{1}{n}$
ZnO	0.511	2.387	0.804	− 1.241
$Zn_{0.97}Ho_{0.03}O$	0.099	4.462	0.635	− 1.061
$Zn_{0.97}Gd_{0.03}O$	0.471	3.743	0.659	− 2.254

Ho doping to 3.138 eV for $Zn_{0.97}Ho_{0.03}O$. At pH = 8, the sample $Zn_{0.97}Ho_{0.03}O$ had the highest removal efficiency of 91%. The experimental data was fitted using the Freundlich and Langmuir isotherm models. The model that fits the experimental results the best is the Freundlich model.

Declarations

References

1. Y. Xia, J. Wang, R. Chen, D. Zhou, L. Xiang, A review on the fabrication of hierarchical ZnO nanostructures for photocatalysis application. Crystals **6**(11), 148 (2016)

2. L. Schmidt-Mende, J.L. MacManus-Driscoll, ZnO–nanostructures, defects, and devices. Mater. Today **10**(5), 40–48 (2007)

3. G. Nagaraju, S.A. Prashanth, M. Shastri, K.V. Yathish, C. Anupama, D. Rangappa, Electrochemical heavy metal detection, photocatalytic, photoluminescence, biodiesel production and antibacterial activities of Ag–ZnO nanomaterial. Mater. Res. Bull. **94**, 54–63 (2017)

4. Z. Nia, Y. Suna, Y. Zhangb, F. Dong, Fabrication, modification and application of $(BiO)_2CO_3$-based photocatalysts: a review. Appl. Surf. Sci. **365**, 314–335 (2016)

5. S. Adhikari, A. Adhikari, S. Ghosh, D. Roy, I. Azahar, D. Basuli, Z. Hossain, Assessment of ZnO-NPs toxicity in maize: an integrative microRNAomic approach. Chemosphere **249**, 126197 (2020)

6. R. Gang, L. Xu, Y. Xia, J. Cai, L. Zhang, S. Wang, R. Li, Fabrication of MoS2 QDs/ZnO nanosheet 0D/2D heterojunction photocatalysts for organic dyes and gaseous heavy metal removal. J. Colloid Interface Sci. **579**, 853–861 (2020)

7. K.H. Choi, S. Jeon, H.K. Kim, A comparison of Ga: ZnO and Ga: ZnO/Ag/Ga: ZnO source/drain electrodes for In–Ga–Zn–O thin film transistors. Mater. Res. Bull. **47**(10), 2915–2918 (2012)

8. A. Kumawat, K.P. Misra, S. Chattopadhyay, Band gap engineering and relationship with luminescence in rare-earth elements doped ZnO: an overview. Mater. Technol. **37**(11), 1595–1610 (2022)

9. B. Thomas, L.K. Alexander, Removal of Pb^{2+} and Cd^{2+} toxic heavy metal ions driven by Fermi level modification in $NiFe_2O_4$–Pd nano hybrids. J. Solid State Chem. **288**, 121417 (2020)

10. F. Fu, Q. Wang, Removal of heavy metal ions from wastewaters: a review. J. Environ. Manag. **92**(3), 407–418 (2011)

11. G. Kim, E.T. Igunnu, G.Z. Chen, A sunlight assisted dual purpose photoelectrochemical cell for low voltage removal of heavy metals and organic pollutants in wastewater. Chem. Eng. J. **244**, 411–421 (2014)

12. X. Zhu, T. Song, Z. Lv, G. Ji, High-efficiency and low-cost α-Fe_2O_3 nanoparticles-coated volcanic rock for Cd (II) removal from wastewater. Process Saf. Environ. Prot. **104**, 373–381 (2016)

13. S. Wadhawan, A. Jain, J. Nayyar, S.K. Mehta, Role of nanomaterials as adsorbents in heavy metal ion removal from waste water: a review. J. Water Process Eng. **33**, 101038 (2020)

14. C.H. Neoh, Z.Z. Noor, N.S.A. Mutamim, C.K. Lim, Green technology in wastewater treatment technologies: integration of membrane bioreactor with various wastewater treatment systems. Chem. Eng. J. **283**, 582–594 (2016)

15. S. Murgolo, F. Petronella, R. Ciannarella, R. Comparelli, A. Agostiano, M.L. Curri, G. Mascolo, UV and solar-based photocatalytic degradation of organic pollutants by nano-sized TiO_2 grown on carbon nanotubes. Catal. Today **240**, 114–124 (2015)

16. C.K. Mbamba, D.J. Batstone, X. Flores-Alsina, S. Tait, A generalised chemical precipitation modelling approach in wastewater treatment applied to calcite. Water Res. **68**, 342–353 (2015)

17. G. Sekaran, S. Karthikeyan, R. Boopathy, P. Maharaja, V.K. Gupta, C. Anandan, Response surface modeling for optimization heterocatalytic Fenton oxidation of persistence organic pollution in high total dissolved solid containing wastewater. Environ. Sci. Pollut. Res. Int. **21**(2), 1489–1502 (2014)

18. S.S. da Silva, O. Chiavone-Filho, E.L. de Barros Neto, E.L. Foletto, Oil removal from produced water by conjugation of flotation and photo-Fenton processes. J. Environ. Manag. **147**, 257–263 (2015)

19. H. Bi, Z. Yin, X. Cao, X. Xie, C. Tan, X. Huang, B. Chen, F. Chen, Q. Yang, X. Bu, X. Lu, L. Sun, H. Zhang, Carbon fiber aerogel made from raw cotton: a novel, efficient and recyclable sorbent for oils and organic solvents. Adv. Mater. **25**(41), 5916–5921 (2013)

20. M. Hasanpour, M. Hatami, Application of three dimensional porous aerogels as adsorbent for removal of heavy metal ions from water/wastewater: a review study. Adv. Colloids Interface. Sci. **284**, 102247 (2020)

21. M.M. Arman, Preparation, characterization and magnetic properties of Sm0.95Ho0.05FeO3 nanoparticles and their application in the purification of water. Appl. Phys. A **129**(1), 1–10 (2023)

22. E.E. Ateia, R. Ramadan, B. Hussein, Studies on multifunctional properties of $GdFe_{1-x}Co_xO_3$ multiferroics. Appl. Phys. A **126**, 1–11 (2020)

23. E.E. Ateia, M.M. Arman, A.T. Mohamed, A facile novel synthesis of $AgCuO_2$ delafossite nanoparticles and evaluation of their antimicrobial activity. Sci. Rep. **13**(1), 3141 (2023)

24. A. Manikandan, E. Manikandan, B. Meenatchi, S. Vadivel, S.K. Jaganathan, R. Ladchumananandasivam, J.S. Aanand, Rare earth element (REE) lanthanum doped zinc oxide (La: ZnO) nanomaterials: synthesis structural optical and antibacterial studies. J. Alloys Compd. **723**, 1155–1161 (2017)

25. R.D. Shannon, Revised effective ionic radii and systematic studies of interatomic distances in halides and chalcogenides. Acta

Crystallogr. Sect. A Cryst. Phys. Diffr. Theor. Gen. Crystallogr. **32**(5), 751–767 (1976)

26. E.E. Ateia, M.A. Ateia, M.M. Arman, Assessing of channel structure and magnetic properties on heavy metal ions removal from water. J. Mater. Sci. Mater. Electron. **33**(11), 8958–8969 (2022)

27. K. Kasirajan, L.B. Chandrasekar, S. Maheswari, M. Karunakaran, P.S. Sundaram, A comparative study of different rare-earth (Gd, Nd, and Sm) metals doped ZnO thin films and its room temperature ammonia gas sensor activity: synthesis, characterization, and investigation on the impact of dopant. Opt. Mater. **121**, 111554 (2021)

28. P. Pascariu, C. Cojocaru, N. Olaru, P. Samoila, A. Airinei, M. Ignat, D. Timpu, Novel rare earth (RE-La, Er, Sm) metal doped ZnO photocatalysts for degradation of Congo-Red dye: synthesis, characterization and kinetic studies. J. Environ. Manag. **239**, 225–234 (2019)

29. A. George, S.K. Sharma, S. Chawla, M.M. Malik, M.S. Qureshi, Detailed of X-ray diffraction and photoluminescence studies of Ce doped ZnO nanocrystals. J. Alloy Compd. **509**(20), 5942–5946 (2011)

30. M.M. Arman, S.I. El-Dek, Role of annealing temperature in tailoring Ce-doped LaFeO$_3$ features. J. Phys. Chem. Solids **152**, 109980 (2021)

31. S. Zhou, K. Potzger, H. Reuther, K. Kuepper, W. Skorupa, M. Helm, J. Fassbender, J. Appl. Phys. **101**, 09H109 (2007)

32. N.H. Hong, J. Sakai, V. Brizé, J. Phys. Condens. Matter **19**, 036219 (2007)

33. Q. Xu, S. Zhou, H. Schmidt, Magnetic properties of ZnO nanopowders. J. Alloy Compd. **487**(1–2), 665–667 (2009)

34. K.H. Mabhouti, M. Karamirad, P. Norouzzadeh, M.M. Golzan, R. Naderali, Measurement of electric and magnetic properties of ZnO nanoparticles in the X-band using Nicolson–Ross–Weir analysis. J. Electron. Mater. **49**(6), 3668–3676 (2020)

35. A. Sundaresan, R. Bhargavi, N. Rangarajan, U. Siddesh, C.N.R. Rao, Phys. Rev. B **74**, 161306R (2006)

36. Q. Xu, H. Schmidt, S. Zhou, K. Potzger, M. Helm, H. Hochmuth, M. Lorenz, A. Setzer, P. Esquinazi, C. Meinecke, M. Grundmann, Appl. Phys. Lett. **92**, 082508 (2008)

37. R. López, R. Gómez, Band-gap energy estimation from diffuse reflectance measurements on sol–gel and commercial TiO$_2$: a comparative study. J. Sol-Gel. Sci. Technol. **61**(1), 1–7 (2012)

38. M.M. Arman, M.K. Ahmed, M.M. El-Masry, Cellulose Acetate polymer spectroscopic study comprised LaFeO$_3$ perovskite and graphene as a UV-to-visible light converter used in several applications. J. Mol. Struct. **1281**, 135153 (2023)

39. A. Rai, A.K. Thakur, Influence of co-substitution driven property tailoring in lanthanum orthoferrites (LaFeO$_3$). Ceram. Int. **43**(16), 13828–13838 (2017)

40. E. Burstein, Anomalous optical absorption limit in InSb. Phys. Rev. **93**(3), 632 (1954)

41. J. Wang, W. Cui, L. Zhu, J. Wang, Q. Wei, Z. Chen, J. Hua, Structural, optical, and magnetic properties of low temperature hydrothermal synthesized (Gd, Al)-codoped ZnO nanoparticles. J. Sol-Gel Sci. Technol. **93**(1), 193–201 (2020)

42. G.L. Kabongo, G.H. Mhlongo, M.S. Dhlamini, Unveiling semiconductor nanostructured based holmium-doped ZnO: structural, luminescent and room temperature ferromagnetic properties. Nanomaterials **11**(10), 2611 (2021)

43. S.K. Ray, Y.K. Kshetri, T. Yamaguchi, T.H. Kim, S.W. Lee, Characterization and multicolor upconversion emission properties of BaMoO$_4$: Yb^{3+}, Ln^{3+} (Ln = Tm, Ho, Tm/Ho) microcrystals. J. Solid State Chem. **272**, 87–95 (2019)

44. I. Ghiloufi, J. El Ghoul, A. Modwi, L. El Mir, Ga-doped ZnO for adsorption of heavy metals from aqueous solution. Mater. Sci. Semicond. Process. **42**, 102–106 (2016)